

## Article

# Thermal Runaway Propagation in Pouch-Type Lithium-Ion Battery Modules: Effects of State of Charge and Initiation Location

So-Jin Kim , Yeong-Seok Yu , Chan-Seok Jeong, Sang-Bum Lee and Yong-Un Na  \*

National Fire Research Institute, 376, Songak-ro, Songak-myeon, Asan-si 31555, Republic of Korea

\* Correspondence: zerokira@korea.kr

## Abstract

The widespread adoption of lithium-ion batteries (LIBs) in electric vehicles (EVs) and energy-storage systems (ESSs) has raised growing concern about fire hazards caused by thermal runaway (TR). While many studies have examined cell-level TR mechanisms, investigations at the module level remain limited despite their importance for safety design. In this study, TR propagation was experimentally analyzed in a 12-cell (2p6s) pouch-type LIB module with EV-grade cells. The state of charge (SOC) and initiation location were the main variables. TR was initiated by a surface-mounted Kapton heating film, with power increased stepwise from 63 W to 141 W at 5-min intervals. Temperature, voltage, and heat release rate (HRR) were continuously monitored. Results showed that higher SOC led to earlier TR onset, shorter vent-to-ignition delay, and stronger combustion with jet flames. Center initiation produced rapid bidirectional propagation with a peak heat release rate (PHRR) of 590 kW and a propagation time of 107 s, whereas edge initiation caused slower unidirectional spread with a PHRR of 105 kW and a propagation time of 338 s. These results demonstrate that both SOC and initiation location critically control TR severity and propagation, providing essential data for EV fire safety evaluation and module design.



Academic Editor: Vilas Pol

Received: 24 September 2025

Revised: 20 October 2025

Accepted: 22 October 2025

Published: 28 October 2025

**Citation:** Kim, S.-J.; Yu, Y.-S.; Jeong, C.-S.; Lee, S.-B.; Na, Y.-U. Thermal Runaway Propagation in Pouch-Type Lithium-Ion Battery Modules: Effects of State of Charge and Initiation Location. *Batteries* **2025**, *11*, 398. <https://doi.org/10.3390/batteries11110398>

**Copyright:** © 2025 by the authors. Licensee MDPI, Basel, Switzerland. This article is an open access article distributed under the terms and conditions of the Creative Commons Attribution (CC BY) license (<https://creativecommons.org/licenses/by/4.0/>).

## 1. Introduction

The global rise in greenhouse gas emissions is accelerating the climate crisis [1,2], thereby increasing the demand for sustainable transportation solutions such as electric vehicles (EVs). According to the International Energy Agency (IEA) *Global EV Outlook 2024*, global EV sales reached approximately 14 million units in 2023, representing a 35% increase from the previous year. The number of EVs in operation has also grown sixfold since 2018, reaching about 40 million units [3]. Nevertheless, as EV adoption expands, fire incidents have also increased [4,5], most of which are attributed to battery thermal runaway (TR) [6,7].

Lithium-ion batteries (LIBs) have been widely adopted in EVs, energy-storage systems (ESSs), and many other applications due to their high operating voltage, high energy density, and long service life [8–11]. However, their safety remains a major concern, as TR can be triggered under abuse conditions such as internal or external short circuits, overcharging, external heating, or mechanical damage [12–15]. Once initiated, TR involves exothermic chemical reactions within the cell, leading to a rapid temperature rise that

may escalate into fire or explosion [16–19]. Owing to these severe consequences, TR is considered a critical safety issue.

With increasing safety concerns, substantial research has been conducted to clarify the mechanisms of TR in LIBs. In many studies, TR was intentionally triggered by overcharging [8], external heating [20–24], or nail penetration [25–27], and the resulting temperature rise and fire behavior were analyzed. In addition, recent studies have focused on the emission of toxic and flammable gases during TR events to provide a more comprehensive assessment of associated hazards [28–33].

Beyond cell-level studies, several works have explored TR propagation at the module level through experiments or simulations [34–39]. Ouyang et al. experimentally investigated the effects of battery gap, state of charge (SOC), and phase change material (PCM) on thermal failure propagation in  $3 \times 3$  LIB modules. They found that larger inter-cell gaps effectively suppressed propagation, whereas higher SOC and the presence of PCM led to more severe propagation behavior. Jie et al. developed and validated a coupled thermal-electrical model to investigate TR propagation in 18,650-type LIB packs. Using nail penetration tests for model calibration, they identified two propagation modes governed by inter-cell thermal contact resistance: a rapid, locally overheated mode and a slower, conduction-dominated mode. The study further showed that smaller inter-cell spacing and higher ambient temperature significantly accelerated TR propagation, providing quantitative insight into pack-level safety design. Amano et al. experimentally investigated TR and gas release of single, double, and four-cell NMC pouch configurations at different SOC inside a 100 L vessel. They found that higher SOC resulted in lower onset temperatures, higher peak pressures, and greater gas generation dominated by CO, CH<sub>4</sub>, and C<sub>2</sub>H<sub>4</sub>.

In parallel, considerable efforts have been devoted to enhancing the thermal safety of battery modules [40–44]. Hu et al. developed a carbon-fiber-oriented composite PCM that enhanced both heat transfer performance and thermal stability, thereby enabling efficient heat dissipation for safer battery operation. Yang et al. proposed a modular thermal management system incorporating a phase-changeable polymeric skeleton to improve both mechanical robustness and thermal uniformity of battery modules. The system exhibited more uniform heat distribution and greater structural stability, thereby enhancing overall safety. Huang et al. investigated the suppression of TR propagation in high-rate cycled lithium-ion pouch cells using different thermal barrier materials. The results revealed that optimized configurations effectively reduced heat transfer and significantly improved thermal safety.

Despite these efforts, research on TR at the module and pack levels remains limited compared with the extensive investigations conducted at the cell level. Understanding how TR propagates between cells is crucial for ensuring the safety of large-scale battery systems, yet most previous studies have concentrated on small modules or simplified configurations. Pouch-type modules, which are widely used in EVs, have been investigated far less than cylindrical ones, and experimental studies employing EV-grade pouch modules remain scarce. This research gap highlights the need for systematic investigations of TR propagation in large-format pouch-type modules, particularly under practical conditions.

In this study, a 12-cell (2p6s) pouch-type module with a configuration representative of practical EV applications was employed to experimentally evaluate TR propagation under realistic conditions. The effects of SOC and initiation location on module-level TR behavior were systematically investigated to provide deeper insights into the underlying propagation phenomena. The results offer fundamental data for developing battery safety technologies and fire mitigation strategies. They also support effective prevention and response to EV fires induced by TR.

## 2. Materials and Methods

To examine TR propagation characteristics in pouch-type LIB modules, six experiments were performed using the same module design. The SOC (50%, 75%, and 100%) and the TR initiation location (edge or center) were selected as the main variables. TR propagation was evaluated based on temperature and voltage data, and representative cases at 50% and 100% SOC were further analyzed for visual observation and heat release rate (HRR) to identify characteristic TR behaviors. The schematic of the experimental setup is shown in Figure 1, and the module specifications and test conditions are summarized in Tables 1 and 2, respectively.

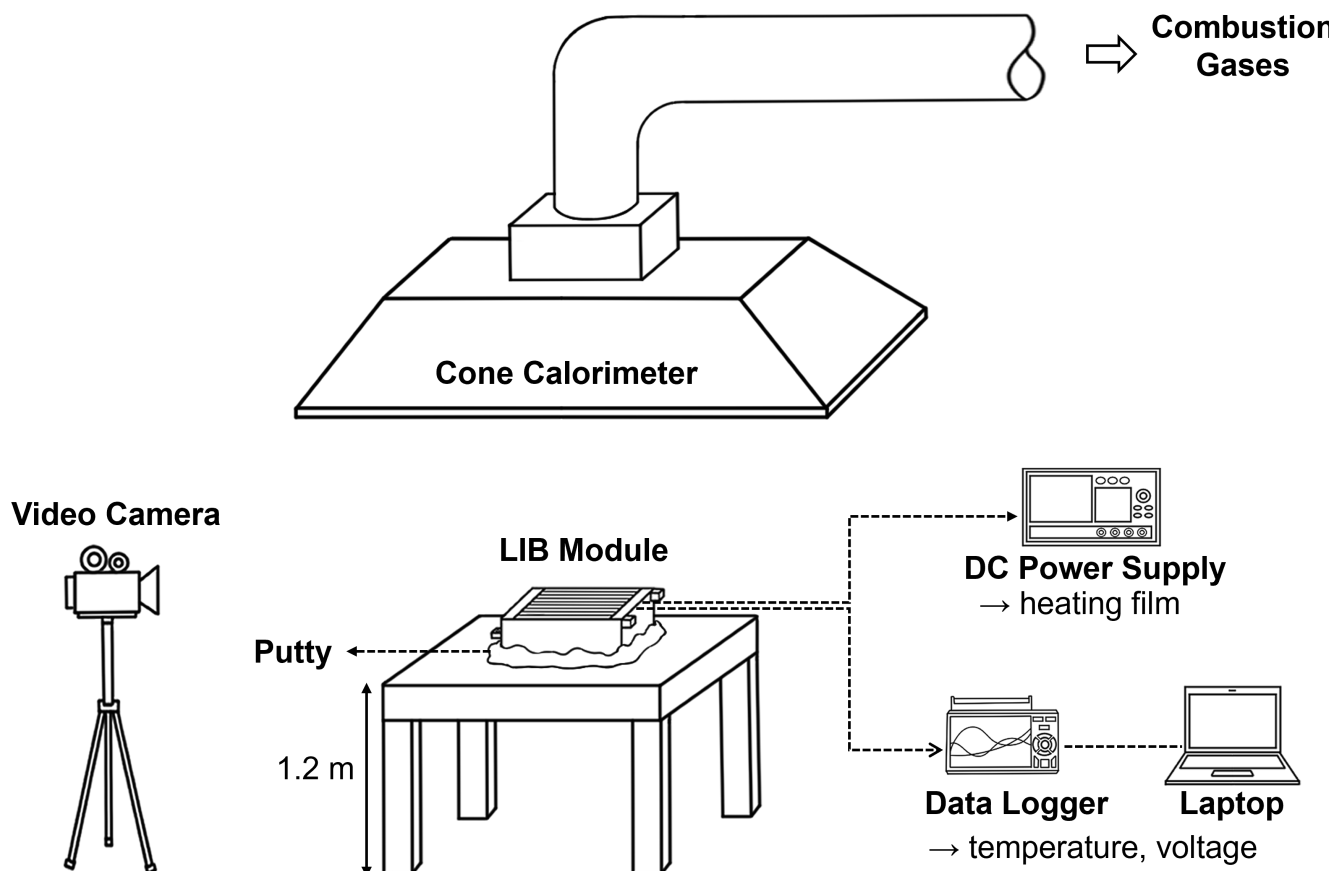


**Figure 1.** Schematic of the experimental setup for TR propagation in pouch-type LIB modules.

**Table 1.** Specifications of the pouch-type LIB module used in the experiments.

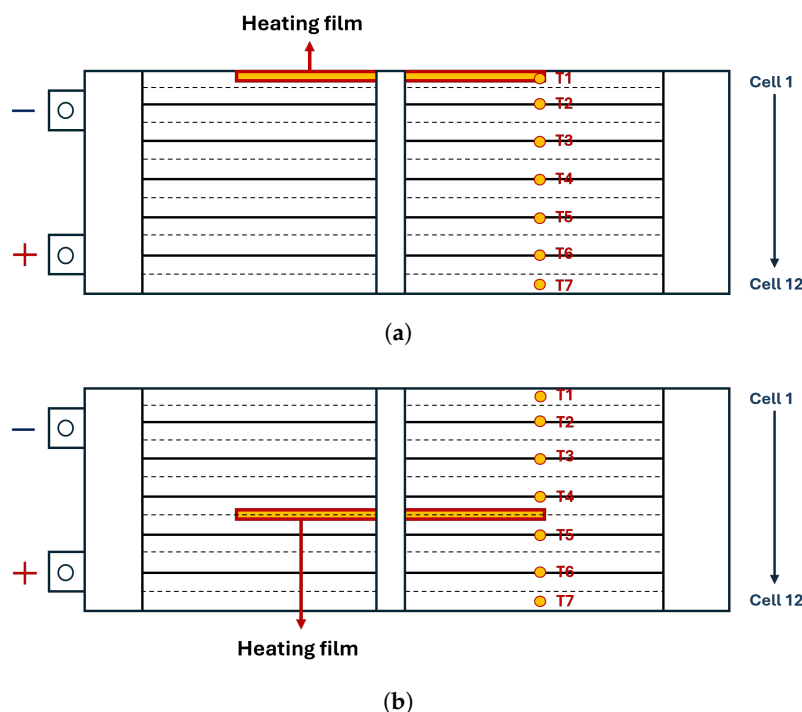
Parameter	Value
Configuration	2p6s
Min/Max voltage	18 V/25.2 V
Nominal voltage	22 V per module
Cell capacity	55.6 Ah
Energy	2.4 kWh
Dimensions	139.7 × 431.8 × 114.3 mm

The pouch-type LIB modules used in this study were NMC 622 modules manufactured by SK ON Co., Ltd. (Seoul, Republic of Korea), which are commonly applied in EVs. Each module consisted of twelve cells arranged in a 2p6s configuration. The individual pouch cells had a nominal capacity of 55.6 Ah and a thickness of approximately 9 mm.

**Table 2.** Experimental conditions for each module with SOC and heating film location.

	SOC (%)	Location of Heating Film
Module 1	50	Edge
Module 2	50	Center
Module 3	75	Edge
Module 4	75	Center
Module 5	100	Edge
Module 6	100	Center

As shown in Figure 2, the cells were numbered sequentially from Cell 1 to Cell 12, starting at the outermost cell on the negative terminal side. Seven K-type thermocouples were attached to the cell surfaces to measure temperature variations, while the module voltage was continuously monitored to identify voltage drops indicating TR onset. To ensure uniform and accurate temperature measurement, the thermocouples were attached to the exposed lower surfaces of the pouch cells, positioned at approximately three quarters of the module width when referenced from the negative and positive tabs. T1 and T7 were attached to the surfaces of Cell 1 and Cell 12, respectively, while T2–T6 were installed between adjacent cell pairs in the 2p6s configuration. Each thermocouple was fixed with high-temperature adhesive tape. Because the sensors were placed beneath the module, they experienced compressive load from the module's weight during testing. Additionally, sealant putty was applied to the underside to prevent ambient air inflow and minimize heat loss, thereby improving temperature measurement accuracy during TR propagation.

**Figure 2.** Thermocouple and heating film positions: (a) Heating film attached to an edge cell, (b) Heating film placed at the center (between Cells 7 and 8).

The heating film location was determined based on the experimental conditions. For Modules 1, 3, and 5, the heater was attached to an edge cell, whereas for Modules 2, 4, and 6, it was positioned between Cells 7 and 8 at the module center. Each heating film was carefully inserted into the narrow gap between adjacent cells or between the outermost cell and the module casing to maintain direct contact with the target cell surface.

The film was precisely aligned with the cell center to ensure uniform heat distribution during heating. A Kapton heating film (200 mm × 40 mm × 0.3 mm) was used, and its temperature was controlled by regulating the output of an RD6012-KA DC power supply (DAQ NET Co., Ltd., Seoul, Republic of Korea).

The heating procedure consisted of five stages, with the input power gradually increased from 63 W to 141 W in 5-min intervals. Signs of TR—such as off-gas emission, voltage drop, and surface temperature rise—were continuously monitored, and heating was immediately stopped once TR onset was detected. The specific power settings for each stage are listed in Table 3. The stepwise power levels were designed to ensure a gradual and controlled temperature rise without triggering immediate combustion. The heating rate was selected to represent typical thermal abuse conditions in EV battery modules, providing a realistic simulation of external heating during TR initiation.

**Table 3.** Heating power applied at each stage of TR initiation.

Stage 1	Stage 2	Stage 3	Stage 4	Stage 5
63 W	86 W	112 W	123 W	141 W

After installing the heating film and thermocouples, a top cover was secured to the battery module to simulate TR conditions in EVs. To measure the HRR, a 5 MW cone calorimeter was installed 1.2 m above the module. The HRR was continuously recorded throughout the test using the oxygen consumption method, and data processing and analysis were performed following the ISO 24473 standard [45].

### 3. Results

#### 3.1. Visual Observation of TR Events

Figure 3 presents sequential images showing the progression of TR events, including venting, ignition, and residual flames. These images allow a direct comparison of the external fire behavior for each module during the experiment.

Analysis of TR ignition characteristics as a function of SOC revealed that ignition occurred earlier at higher SOC after shorter venting periods. In Modules 5 and 6 (100% SOC), ignition occurred almost immediately after venting onset, accompanied by rapid flame ejection. In contrast, Modules 1 and 2 (50% SOC) showed a distinct delay between venting and ignition, and the resulting flames appeared as fireballs. This behavior is attributed to the lower thermal stability of cathode materials at high SOC, where increased lithium extraction leads to greater emission of flammable gases such as CO, CH<sub>4</sub>, and C<sub>2</sub>H<sub>4</sub> [32]. Under these conditions, cell temperature reached the ignition threshold more rapidly, resulting in shorter ignition times.

Flame morphology varied significantly depending on the SOC. Flames in the 50% SOC modules were noticeably weaker than those in the 100% SOC modules. Modules 5 and 6 (100% SOC) exhibited distinct jet flames, whereas no such feature was observed in Modules 1 and 2 (50% SOC). Flame morphology was also affected by the heating film location. Edge heating produced a unidirectional jet flame, while central heating between Cells 7 and 8 generated a bidirectional jet flame, indicating that central initiation facilitated TR propagation in both directions. This directional influence of heating location was further confirmed by temperature and voltage data from each module.

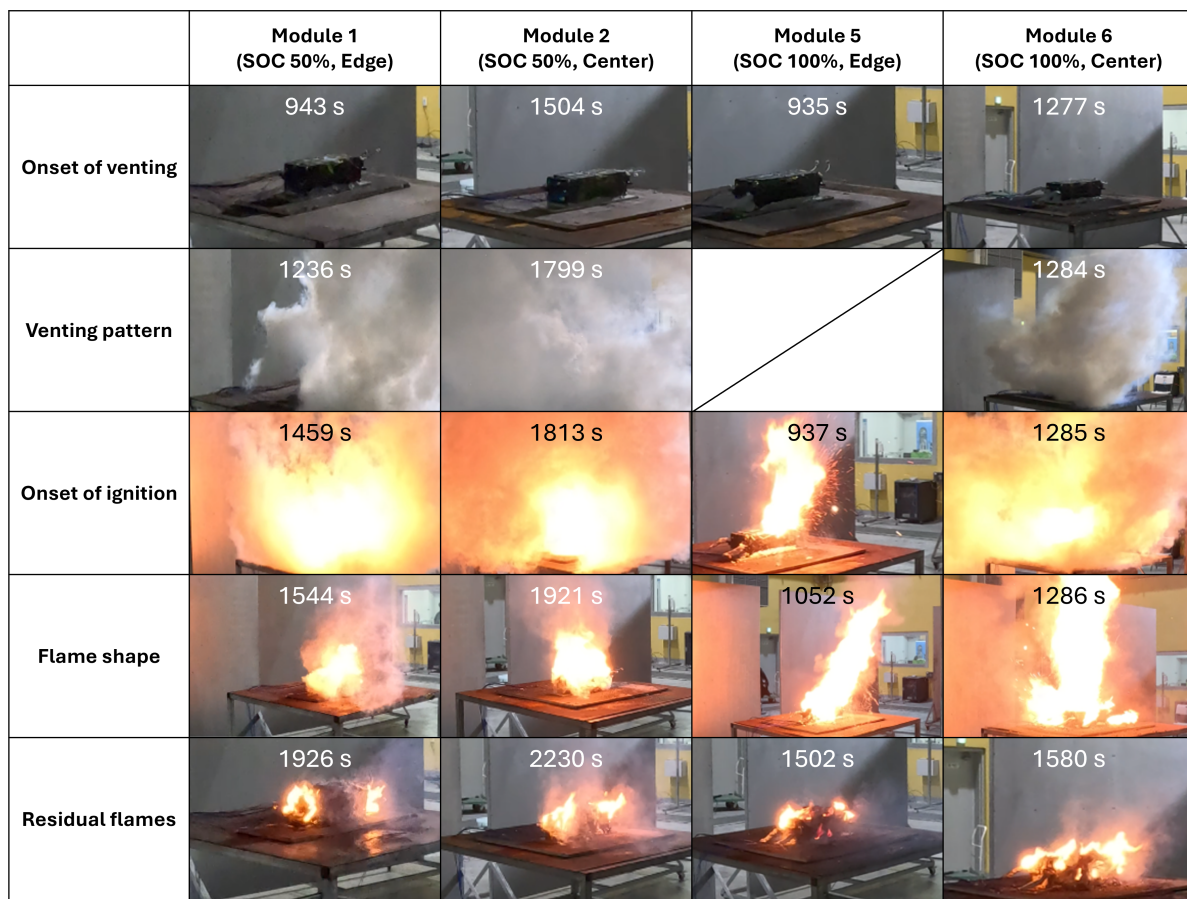


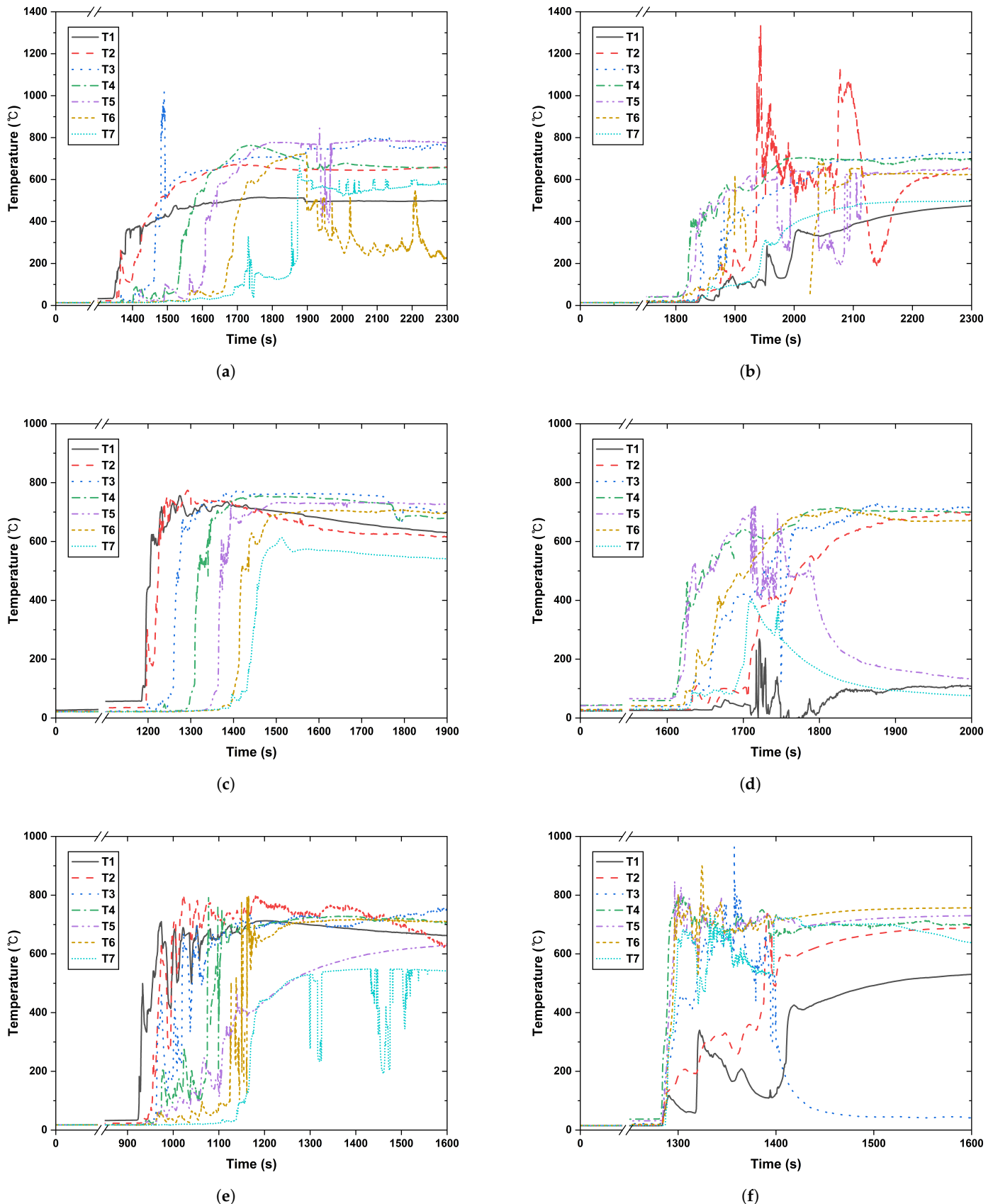
**Figure 3.** Sequential images showing TR ignition and external fire for each module.

### 3.2. Thermal Runaway Propagation Analysis Based on Temperature and Voltage Drop

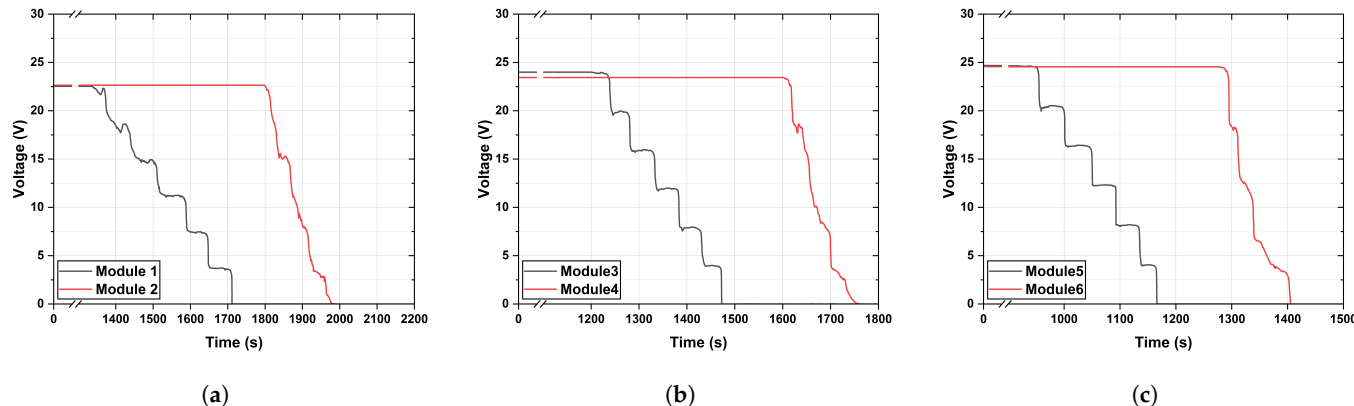
Figures 4 and 5 show the module temperature and voltage profiles over time. In Figure 4, some temperature channels showed missing or noisy signals caused by thermocouple degradation. These anomalies did not represent actual physical behavior and were retained as recorded but excluded from the result interpretation. This signal loss occurred because several thermocouples were directly exposed to intense flames during the later stage of TR, causing overheating and wire damage. Since these anomalies appeared after the onset of TR—when combustion became most intense—they did not affect the determination of the TR initiation point, which was identified from the temperature rise in each cell pair. Therefore, the missing or noisy data had no impact on the analysis of key parameters, including the TR initiation location and onset timing.

Table 4 summarizes the TR onset times for each module, while Table 5 shows the time intervals between consecutive TR events for different module configurations. As noted earlier, the modules were configured in a 2p6s arrangement, where each parallel-connected cell pair shared the same voltage. Accordingly, TR analysis was conducted at the cell-pair level instead of the individual-cell level. The onset of TR was determined from voltage drops, and temperature data were used to identify the specific cell pairs where TR occurred.

In Figure 4, the onset of surface temperature rise was clearly identified for each module. Under the same initiation conditions, edge-initiated modules (Modules 1, 3, and 5) showed earlier heating than center-initiated modules (Modules 2, 4, and 6). In both initiation types, higher SOC resulted in faster surface temperature rise, consistent with the accelerated thermal response at higher SOC. This tendency is attributed to the lower heat input required to trigger TR in edge-initiated modules, where only one cell is in direct contact with the heating film, compared with two cells in center-initiated modules.



**Figure 4.** Temperature profiles of each module over time: (a) Module 1, (b) Module 2, (c) Module 3, (d) Module 4, (e) Module 5, (f) Module 6.



**Figure 5.** Voltage profiles over time for each module: (a) Modules 1 and 2, (b) Modules 3 and 4, (c) Module 5 and 6.

Before analyzing TR events in detail, the voltage drop profiles in Figure 5 were examined. In Modules 1, 3, and 5, where TR was initiated at the outermost cells, repeated voltage plateaus appeared after the initial drop. In Modules 2, 4, and 6, where TR was initiated near the center, these plateaus were comparatively indistinct. This difference originated from the heating film location, which influenced the directionality of TR propagation. When TR was initiated at the outer edge of the module, it propagated unidirectionally, with sequential TR events occurring at relatively consistent intervals. Conversely, when TR was initiated near the center, it propagated bidirectionally, causing multiple cells to undergo TR in rapid succession. Because a voltage drop typically marks the onset of TR, simultaneous TR events across multiple cells likely obscured the voltage plateaus.

At the onset of voltage drop, a brief voltage dip followed by partial recovery was observed. This behavior is attributed to electrical instability, internal circuit disruption, and subsequent energy redistribution within the module during TR [46].

**Table 4.** Sequential TR propagation in Modules 1–6: cell locations and TR onset times.

	Module 1 (SOC 50%, Edge)	Module 2 (SOC 50%, Center)	Module 3 (SOC 75%, Edge)	Module 4 (SOC 75%, Center)	Module 5 (SOC 100%, Edge)	Module 6 (SOC 100%, Center)
First TR	Cell pair (TR onset) Time (s)	Cell 1–Cell 2 1370	Cell 7–Cell 8 1802	Cell 1–Cell 2 1225	Cell 7–Cell 8 1612	Cell 1–Cell 2 952
Second TR	Cell pair (TR onset) Time (s)	Cell 3–Cell 4 1427	Cell 5–Cell 6 1823	Cell 3–Cell 4 1269	Cell 9–Cell 10 1635	Cell 3–Cell 4 996
Third TR	Cell pair (TR onset) Time (s)	Cell 5–Cell 6 1500	Cell 9–Cell 10 1857	Cell 5–Cell 6 1321	Cell 5–Cell 6 1652	Cell 5–Cell 6 1047
Fourth TR	Cell pair (TR onset) Time (s)	Cell 7–Cell 8 1581	Cell 3–Cell 4 1875	Cell 7–Cell 8 1371	Cell 11–Cell 12 1673	Cell 7–Cell 8 1091
Fifth TR	Cell pair (TR onset) Time (s)	Cell 9–Cell 10 1645	Cell 11–Cell 12 1910	Cell 9–Cell 10 1419	Cell 3–Cell 4 1698	Cell 9–Cell 10 1133
Sixth TR	Cell pair (TR onset) Time (s)	Cell 11–Cell 12 1708	Cell 1–Cell 2 1940	Cell 11–Cell 12 1461	Cell 1–Cell 2 1730	Cell 11–Cell 12 1164

**Table 5.** Time intervals between successive TR events for each module configuration.

Interval (s)	Module 1 (SOC 50%, Edge)	Module 2 (SOC 50%, Center)	Module 3 (SOC 75%, Edge)	Module 4 (SOC 75%, Center)	Module 5 (SOC 100%, Edge)	Module 6 (SOC 100%, Center)
Interval 1 (TR <sub>2</sub> – TR <sub>1</sub> )	57	21	44	23	44	20
Interval 2 (TR <sub>3</sub> – TR <sub>2</sub> )	72	34	52	17	51	7
Interval 3 (TR <sub>4</sub> – TR <sub>3</sub> )	81	17	50	21	44	23
Interval 4 (TR <sub>5</sub> – TR <sub>4</sub> )	64	35	48	25	42	15
Interval 5 (TR <sub>6</sub> – TR <sub>5</sub> )	63	31	42	32	31	42
Mean Interval (s)	68	28	47	24	42	21
Total Propagation Time (s)	338	139	236	118	212	107

According to the data presented in Tables 4 and 5, TR in Modules 1, 3, and 5 was initiated at the outermost cells (Cell 1–2) and propagated unidirectionally along the cell array with relatively consistent intervals. Among these, Module 1 (50% SOC) showed the slowest propagation, with a mean interval of 68 s and a total propagation time of 338 s. As SOC increased to 75% (Module 3) and 100% (Module 5), the mean intervals decreased to 47 s and 42 s, respectively, and the total propagation times were shortened to 236 s and 212 s, indicating that propagation accelerated with increasing SOC.

In contrast, TR in Modules 2, 4, and 6 was initiated at the module center (Cells 7–8) and propagated bidirectionally. Module 2 (50% SOC) and Module 4 (75% SOC) exhibited mean intervals of 28 s and 24 s, respectively, whereas Module 6 (100% SOC) showed the shortest interval (21 s) and the fastest total propagation time (107 s). Thus, both SOC and initiation location strongly influenced the direction and rate of TR propagation.

The progressive shortening of TR intervals with increasing SOC is attributed to the greater internal energy of high-SOC cells and their enhanced electrode reactivity. As the SOC increases, the trigger temperature for TR decreases, and the exothermic reactions intensify, releasing more heat during decomposition. The heat transferred from the preceding runaway cell therefore accelerates the temperature rise of neighboring cells, reducing the time required to reach the onset and resulting in faster overall propagation [47].

### 3.3. Heat Release Rate Analysis for Individual Modules

In this study, HRR was considered a key parameter for evaluating fire intensity and understanding TR behavior. Figure 6 shows the HRR evolution during the experiments, while Figure 7 compares the peak HRR (PHRR) and total heat release (THR) among the four modules. Table 6 lists the corresponding PHRR and THR values for each module.

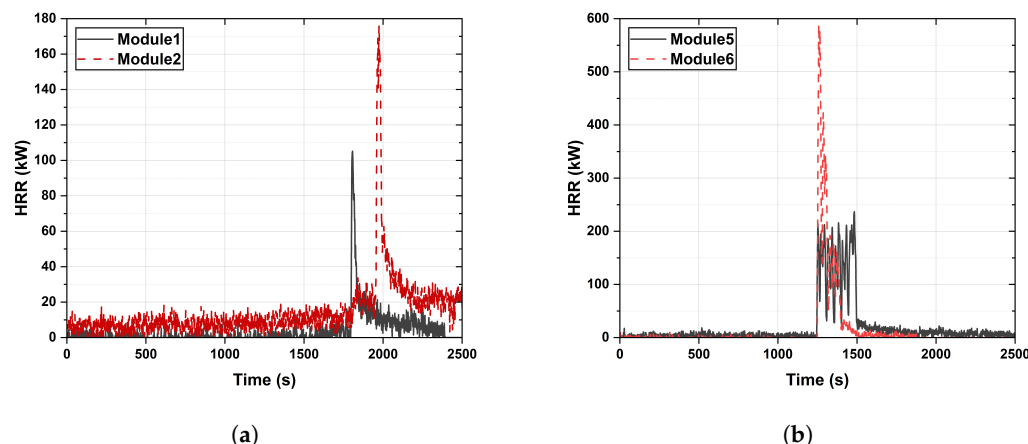


**Figure 6.** HRR profiles of module over time: (a) Modules 1 and 2, (b) Modules 5 and 6.

As shown in Figure 6, Module 5 displayed multiple sharp HRR peaks over time, corresponding to sequential TR events in individual cells. In contrast, Module 6 exhibited the highest HRR during the initial TR event, followed by a gradual decline. Modules 1 and 2 (SOC 50%) showed no significant difference in HRR profiles with respect to initiation location, owing to the lower SOC that limited heat generation during each TR event. These results indicate that Modules 1 and 2 released considerably less heat than Modules 5 and 6, as supported by the PHRR and THR data in Figure 7 and Table 6.

The analysis presented in Figure 7 and Table 6 consistently demonstrates that both PHRR and THR increased with higher SOC levels. These results demonstrate that greater stored energy leads to higher heat release during TR events.

Furthermore, the location of TR initiation had a significant influence on both PHRR and THR. Across all SOC levels, modules ignited at the center exhibited higher PHRR

values than those ignited at the edge. At 50% SOC, the PHRR of the centrally ignited module was about 1.7 times higher than that of the edge-ignited module, whereas at 100% SOC this difference increased to nearly 2.5 times. This trend aligns with the observation that edge ignition leads to sequential TR propagation and consequently lower PHRR. Conversely, center ignition triggered rapid TR propagation across multiple cells, resulting in higher PHRR within a shorter time period.

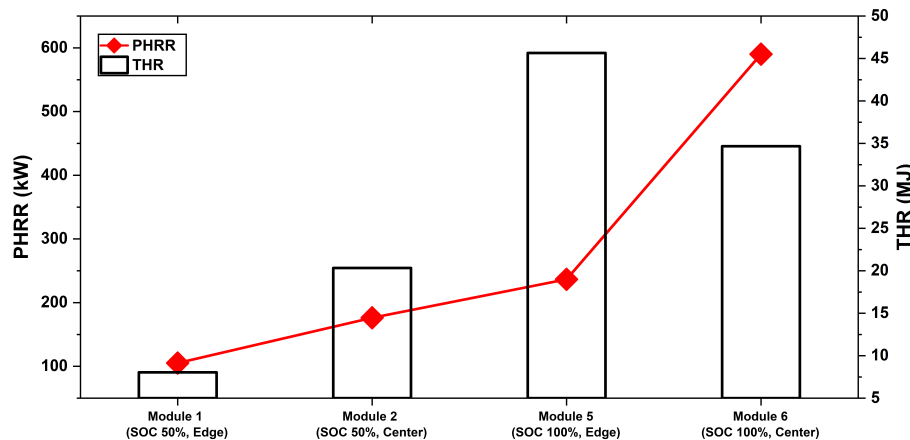


**Figure 7.** Comparison of PHRR and THR among Modules 1, 2, 5 and 6.

**Table 6.** PHRR and THR for each module under different SOC levels and TR initiation locations.

	Module 1 (SOC 50%, Edge)	Module 2 (SOC 50%, Center)	Module 5 (SOC 100%, Edge)	Module 6 (SOC 100%, Center)
PHRR (kW)	105.18	176.25	236.62	590.15
THR (MJ)	8.04	20.34	45.65	34.67

A detailed comparison of THR revealed significant variations with SOC and initiation locations. At 50% SOC, Module 2 released approximately 2.5 times more heat than Module 1, while at 100% SOC, Module 5 released approximately 1.3 times more heat than Module 6. This observation suggests that higher SOC promotes stronger combustion sustained for a longer duration and resulting in greater THR. Notably, the SOC effect was more pronounced under edge ignition. Module 5 exhibited approximately 5.7 times greater THR than Module 1, whereas under center ignition, Module 6 showed only about 1.7 times greater THR than Module 2. These results indicate that heat release behavior during TR varied significantly with both SOC and initiation location, and the SOC effect was stronger under edge ignition. This difference can be attributed to the propagation modes, edge ignition produced sequential TR propagation that allows the SOC effect to accumulate over time and amplify THR differences. In contrast, center ignition triggered near-simultaneous TR in multiple cells, leading to rapid but less SOC-dependent heat release and consequently smaller THR differences.

#### 4. Conclusions

This study investigated TR in pouch-type LIB modules, focusing on cell-to-cell propagation with SOC and initiation location (center or edge) as the main variables. Six experiments were conducted, and the main findings are summarized below.

1. Visual observations of venting onset and flame characteristics revealed that higher SOC levels caused earlier venting and ignition and significantly shortened venting-to-ignition intervals. Additionally, high-SOC modules exhibited intense jet-flame combustion, whereas low-SOC modules showed delayed ignition with weaker, fireball-type flames.

2. Analysis of temperature and voltage profiles showed that higher-SOC modules exhibited faster temperature rise and more rapid TR propagation. Voltage profiles exhibited abrupt drops in parallel-connected cell pairs, enabling the identification of TR onset. When ignition occurred at the module center, sequential voltage drops appeared across multiple cells in quick succession, indicating faster and more extensive TR propagation.
3. Based on the experimental results, edge-ignited modules exhibited unidirectional propagation with relatively consistent intervals between successive events, while center-ignited modules exhibited bidirectional propagation with faster overall spread. A higher SOC further shortened the intervals between successive TR events and reduced the total propagation time. These results demonstrate that both SOC and ignition location play critical roles in determining TR propagation dynamics.
4. The HRR results showed that both PHRR and THR increased with higher SOC levels. The initiation location was also a critical factor, as center-ignited modules generally exhibited higher PHRR than edge-ignited modules. Moreover, the effect of SOC on THR became more pronounced under edge-ignition conditions.

These results enhance the understanding of TR propagation mechanisms in pouch-type LIB modules and provide valuable insights for future safety evaluations as well as the development of effective fire mitigation strategies.

**Author Contributions:** Conceptualization, S.-J.K. and Y.-U.N.; Methodology, Y.-U.N.; Validation, S.-J.K. and Y.-U.N.; Software, S.-J.K.; Formal analysis, S.-J.K.; Investigation, S.-J.K., Y.-S.Y., C.-S.J., S.-B.L. and Y.-U.N.; Resources, Y.-U.N.; Data curation, S.-J.K.; Writing-original draft, S.-J.K.; Writing-review and editing, S.-J.K. and Y.-U.N.; Visualization, S.-J.K.; Supervision, Y.-U.N.; Project administration, Y.-U.N.; Funding acquisition, Y.-U.N. All authors have read and agreed to the published version of the manuscript.

**Funding:** This research was supported by the Technology and Development to Support Firefighting Activities (276000048) funded by National Fire Agency. This research was also supported by the Korean Society of Automotive Engineers (KSAE) grant.

**Data Availability Statement:** The original contributions presented in this study are included in the article. Further inquiries can be directed to the corresponding author.

**Conflicts of Interest:** The authors declare no conflict of interest.

## Abbreviations

The following abbreviations are used in this manuscript:

EV	Electric vehicle
IEA	International energy agency
TR	Thermal runaway
LIB	Lithium-ion battery
ESS	Energy-storage system
SOC	State of charge
PCM	Phase change material
HRR	Heat release rate
PHRR	Peak heat release rate
THR	Total heat release

## References

1. Filonchyk, M.; Peterson, M.P.; Zhang, L.; Hurynovich, V.; He, Y. Greenhouse gases emissions and global climate change: Examining the influence of CO<sub>2</sub>, CH<sub>4</sub>, and N<sub>2</sub>O. *Sci. Total Environ.* **2024**, *935*, 173359. [CrossRef] [PubMed]
2. Althor, G.; Watson, J.E.M.; Fuller, R.A. Global mismatch between greenhouse gas emissions and the burden of climate change. *Sci. Rep.* **2016**, *6*, 20281. [CrossRef]
3. IEA. Global EV Outlook 2024 (Moving Towards Increased Affordability). 2024. Available online: <https://www.iea.org/reports/global-ev-outlook-2024> (accessed on 13 May 2025).
4. Hassan, M.K.; Hameed, N.; Hossain, D.; Hasnat, M.R.; Douglas, G.B.; Pathirana, S.; Rahnamayiezekavat, P.; Saha, S. Fire incidents, trends, and risk mitigation framework of electrical vehicle cars in Australia. *Fire* **2023**, *6*, 325. [CrossRef]
5. He, H.; Sun, F.; Wang, Z.; Lin, C.; Zhang, C.; Xiong, R.; Deng, J.; Zhu, X.; Xie, P.; Zhang, S.; et al. China's battery electric vehicles lead the world: Achievements in the technology system architecture and technological breakthroughs. *Green Energy Intell. Transp.* **2022**, *1*, 100020. [CrossRef]
6. Lai, X.; Yao, J.; Jin, C.; Feng, X.; Wang, H.; Xu, C.; Zheng, Y. A Review of lithium-ion battery failure Hazards: Test standards, accident analysis, and safety suggestions. *Batteries* **2022**, *8*, 248. [CrossRef]
7. Sun, P.; Bisschop, R.; Niu, H.; Huang, X. A review of battery fires in electric vehicles. *Fire Technol.* **2020**, *56*, 1361–1410. [CrossRef]
8. Park, M.W.; Jang, W.B.; Hong, S.H.; Choi, D.M. Characteristics of thermal runaway generation of pouch-type lithium-ion batteries by overcharging. *Fire Sci. Eng.* **2020**, *34*, 8–13. [CrossRef]
9. Hua, Y.; Zhou, S.; Huang, Y.; Liu, X.; Ling, H.; Zhou, X.; Zhang, C.; Yang, S. Sustainable value chain of retired lithium-ion batteries for electric vehicles. *J. Power Sources* **2020**, *478*, 228753. [CrossRef]
10. Liao, Z.; Zhang, S.; Li, K.; Zhang, G.; Habetler, T.G. A survey of methods for monitoring and detecting thermal runaway of lithium-ion batteries. *J. Power Sources* **2019**, *436*, 226879. [CrossRef]
11. Weber, R.; Genovese, M.; Louli, A.J.; Hames, S.; Martin, C.; Hill, I.G.; Dahn, J.R. Long cycle life and dendrite-free lithium morphology in anode-free lithium pouch cells enabled by a dual-salt liquid electrolyte. *Nat. Energy* **2019**, *4*, 683–689. [CrossRef]
12. Doughty, D.H.; Roth, E.P. A general discussion of li ion battery safety. *Electrochem. Soc. Interface* **2012**, *21*, 37. [CrossRef]
13. Wang, Q.; Mao, B.; Stolarov, S.I.; Sun, J. A review of lithium ion battery failure mechanisms and fire prevention strategies. *Prog. Energy Combust. Sci.* **2019**, *73*, 95–131. [CrossRef]
14. Chen, Y.; Kang, Y.; Zhao, Y.; Wang, L.; Liu, J.; Li, Y.; Liang, Z.; He, X.; Li, X.; Tavajohi, N.; et al. A review of lithium-ion battery safety concerns: The issues, strategies, and testing standards. *J. Energy Chem.* **2021**, *59*, 83–99. [CrossRef]
15. Mao, B.; Huang, P.; Chen, H.; Wang, Q.; Sun, J. Self-heating reaction and thermal runaway criticality of the lithium ion battery. *Int. J. Heat Mass Transf.* **2020**, *149*, 119178. [CrossRef]
16. ANSI/CAN/UL 9540A; Test Method for Evaluating Thermal Runaway Fire Propagation in Battery Energy Storage Systems. Underwriters Laboratories: Northbrook, IL, USA, 2019.
17. Liu, K.; Liu, Y.; Lin, D.; Pei, A. Materials for lithium-ion battery safety. *Mater. Sci.* **2018**, *4*, eaas9820. [CrossRef] [PubMed]
18. Larsson, F.; Andersson, P.; Blomqvist, P.; Lofen, A.; Mellander, B.E. Characteristics of lithium-ion batteries during fire tests. *J. Power Sources* **2014**, *271*, 414–420. [CrossRef]
19. Lyu, P.; Liu, X.; Qu, J.; Zhao, J.; Huo, Y.; Qu, Z.; Rao, Z. Recent advances of thermal safety of lithium ion battery for energy storage. *Energy Storage Mater.* **2020**, *31*, 195–220. [CrossRef]
20. Gagnon, L.; Zeng, D.; Ditch, B.; Wang, Y. Cell-level thermal runaway behavior of large-format Li-ion pouch cells. *Fire Saf. J.* **2023**, *140*, 103904. [CrossRef]
21. Wang, P.; Xu, C.; Jiang, W.; Wang, W.; Liu, L.; Gu, J.; Fan, Z.; Zhang, M.; Huang, J.; Jiang, F.; et al. Experimental study on thermal runaway venting behaviour of LiNi<sub>0.8</sub>Co<sub>0.1</sub>Mn<sub>0.1</sub>O<sub>2</sub> pouch cell under different sealing edge directions. *J. Power Sources* **2024**, *621*, 235327. [CrossRef]
22. Zou, K.; Lu, S.; Chen, X.; Gao, E.; Cao, Y.; Bi, Y. Thermal and gas characteristics of large-format LiNi<sub>0.8</sub>Co<sub>0.1</sub>Mn<sub>0.1</sub>O<sub>2</sub> pouch power cell during thermal runaway. *J. Energy Storage* **2021**, *39*, 102609. [CrossRef]
23. Lee, H.S.; Hong, S.H.; Lee, J.H.; Park, M.W. Analysis of effect of surface temperature rise rate of 72.5 Ah NCM pouch-type lithium-ion battery on thermal runaway trigger time. *J. Korean Soc. Saf.* **2021**, *36*, 1–9
24. Kim, D.; Sim, I.; Park, S. Analysis of thermal runaway in pouch-type lithium-ion batteries using particle image velocimetry. *Int. J. Energy Res.* **2023**, *2023*, 5568642. [CrossRef]
25. Feng, X.; Zhang, F.; Huang, W.; Peng, Y.; Xu, C.; Ouyang, M. Mechanism of internal thermal runaway propagation in blade batteries. *J. Energy Chem.* **2024**, *89*, 184–194. [CrossRef]
26. Zhang, F.; Feng, X.; Xu, C.; Jiang, F.; Ouyang, M. Thermal runaway front in failure propagation of long-shape lithium-ion battery. *Int. J. Heat Mass Transf.* **2022**, *182*, 121928. [CrossRef]
27. Wang, H.; Yang, Z.; Jiang, C.; Ji, Z.; Zhu, Z.X. Internal temperature and flame jet characteristics during thermal runaway triggered by nail penetration for NCM811 lithium-ion battery. *J. Therm. Anal. Calorim.* **2022**, *147*, 14925–14938. [CrossRef]

28. Bugryniec, P.J.; Resendiz, E.G.; Nwophoke, S.M.; Khanna, S.; James, C.; James, C.; Brown, S.F. Review of gas emissions from lithium-ion battery thermal runaway failure—Considering toxic and flammable compounds. *J. Energy Storage* **2024**, *87*, 111288. [[CrossRef](#)]
29. Larsson, F.; Andersson, P.; Blomqvist, P.; Mellander, B.E. Toxic fluoride gas emissions from lithium-ion battery fires. *Sci. Rep.* **2017**, *7*, 10018. [[CrossRef](#)]
30. Xu, C.; Fan, Z.; Zhang, M.; Wang, P.; Wang, H.; Jin, C.; Peng, Y.; Jiang, F.; Feng, X.; Ouyang, M. A comparative study of the venting gas of lithium-ion batteries during thermal runaway triggered by various methods. *Cell Rep. Phys. Sci.* **2023**, *4*, 101705. [[CrossRef](#)]
31. Qiu, M.; Liu, J.; Cong, B.; Cui, Y. Research progress in thermal runaway vent gas characteristics of li-ion battery. *Batteries* **2023**, *9*, 411. [[CrossRef](#)]
32. Amano, K.O.A.; Hahn, S.K.; Butt, N.; Vorwerk, P.; Gimadieva, E.; Tschirschitz, R.; Rappsilber, T.; Krause, U. Composition and explosibility of gas emissions from lithium-ion batteries undergoing thermal runaway. *Batteries* **2023**, *9*, 300. [[CrossRef](#)]
33. Koch, S.; Fill, A.; Birke, K.P. Comprehensive gas analysis on large scale automotive lithium-ion cells in thermal runaway. *J. Power Sources* **2018**, *398*, 106–112. [[CrossRef](#)]
34. Ouyang, D.; Weng, J.; Hu, J.; Chen, M.; Huang, Q.; Wang, J. Experimental investigation of thermal failure propagation in typical lithium-ion battery modules. *Thermochim. Acta* **2019**, *676*, 205–213. [[CrossRef](#)]
35. Jia, Y.; Uddin, M.; Li, Y.; Xu, J. Thermal runaway propagation behavior within 18,650 lithium-ion battery packs: A modeling study. *J. Energy Storage* **2020**, *31*, 101668. [[CrossRef](#)]
36. Ouyang, D.; Liu, J.; Chen, M.; Weng, J.; Wang, J. Thermal failure propagation in lithium-ion battery modules with various shapes. *Appl. Sci.* **2018**, *8*, 1263. [[CrossRef](#)]
37. Lamb, J.; Orendorff, C.J.; Steele, L.A.M.; Spangler, S.W. Failure propagation in multi-cell lithium ion batteries. *J. Power Sources* **2015**, *283*, 517–523. [[CrossRef](#)]
38. Aiello, L.; Hanzu, I.; Gstrein, G.; Ewert, E.; Ellersdorfer, C.; Sinz, W. Analysis and investigation of thermal runaway propagation for a mechanically constrained lithium-ion pouch cell module. *Batteries* **2021**, *7*, 49. [[CrossRef](#)]
39. Amano, K.O.A.; Hahn, S.K.; Tschirschitz, R.; Rappsilber, T.; Krause, U. An experimental investigation of thermal runaway and gas release of NMC lithium-ion batteries depending on the state of charge level. *Batteries* **2022**, *8*, 41. [[CrossRef](#)]
40. Hu, J.; Yao, Z.; Chen, A.; Xiao, C.; Zhang, G.; Yang, X. High thermal-conductive phase change material by carbon fiber orientation for thermal management and energy conversion application. *Appl. Therm. Eng.* **2025**, *265*, 125566. [[CrossRef](#)]
41. Yang, X.; Huang, R.; Yao, Z.; Chang, G. Modular assembly strategy to construct lightweight thermal management system by developing high-stable phase change material units. *Chem. Eng. Sci.* **2024**, *299*, 120529. [[CrossRef](#)]
42. Huang, Y.; Shen, X.; Zhao, Y.; Wang, J.; Cao, Y.; Bai, W.; Fan, Y.; Lu, Y.; Wang, Z. Investigation on the inhibition mechanism of thermal runaway propagation in high-rate cycling lithium-ion pouch cells. *Process Saf. Environ. Prot.* **2025**, *197*, 106975. [[CrossRef](#)]
43. Tan, W.; Ren, L.; Tian, T.; Ma, K.; Wang, S.; Zhang, Z. Thermal runaway propagation and suppression in mobile energy storage lithium battery module. *J. Energy Storage* **2025**, *131*, 117615. [[CrossRef](#)]
44. Xie, J.; Li, J.; Li, C.; Huang, X.; Zhang, G.; Yang, X. Multi-level passive-active thermal control for battery thermal runaway prevention and suppression in electric vehicles. *eTransportation* **2025**, *26*, 100467. [[CrossRef](#)]
45. ISO 24473:2008; Fire Tests—Open Calorimetry—Measurement of the Rate of Production of Heat and Combustion Products for Fires of up to 40 MW. International Organization for Standardization (ISO): Geneva, Switzerland, 2008.
46. Zhou, Z.; Li, M.; Zhou, X.; Ju, X.; Yang, L. Investigating thermal runaway characteristics and trigger mechanism of the parallel lithium-ion battery. *Appl. Energy* **2023**, *349*, 121690. [[CrossRef](#)]
47. Zhu, M.; Zhang, S.; Zhao, L.; Chen, M. Experimental and analytical investigation on the thermal runaway propagation characteristics of lithium-ion battery module with NCM pouch cells under various state of charge and spacing. *J. Energy Storage* **2023**, *72*, 108380. [[CrossRef](#)]

**Disclaimer/Publisher’s Note:** The statements, opinions and data contained in all publications are solely those of the individual author(s) and contributor(s) and not of MDPI and/or the editor(s). MDPI and/or the editor(s) disclaim responsibility for any injury to people or property resulting from any ideas, methods, instructions or products referred to in the content.